Dispersion Characteristics and Rheology of Organoclay Nanocomposites Based on a Segmented Main-Chain Liquid-Crystalline Polymer Having Pendent Pyridyl Group

Wenyi Huang and Chang Dae Han*

Department of Polymer Engineering, The University of Akron, Akron, Ohio 44325

Received July 6, 2005; Revised Manuscript Received October 27, 2005

ABSTRACT: The dispersion characteristics and rheology of organoclay nanocomposites based on a thermotropic liquid-crystalline polymer (TLCP) having pendent functional group were investigated using X-ray diffraction (XRD), transmission electron microscopy (TEM), and oscillatory shear rheometry. For the study, a segmented main-chain TLCP having pendent pyridyl group (PyHQ12) was synthesized and, for comparison, another segmented main-chain TLCP having pendent phenylsulfonyl group (PSHQ12) was synthesized, both TLCPs having the identical chemical structure for the main-chain backbone. The differences in phase transition temperature and rheological behavior observed between PyHQ12 and PSHQ12 are explained in terms of the self-associating characteristics of the pendent pyridyl group in PyHQ12. PyHQ12 and PSHQ12 were used to prepare nanocomposites with two commercial organoclays: one (Cloisite 30B) was natural clay (montmorillonite) treated with a surfactant (MT2EtOH) having hydroxyl groups, and the other (Cloisite 20A) was montmorillonite treated with a surfactant (2M2HT) having no polar group. The following observations have been made. (i) PyHQ12/Cloisite 30B nanocomposite has featureless XRD patterns and a very high degree of dispersion of Cloisite 30B aggregates as determined from TEM. (ii) PyHQ12/Cloisite 20A nanocomposite has a conspicuous XRD reflection peak giving rise to an increase of gallery distance by 0.3 nm from the gallery distance of 3.1 nm for Cloisite 20A and intercalation of Cloisite 20A aggregates as determined from TEM. (iii) PSHQ12/Cloisite30B nanocomposite also has a conspicuous XRD reflection peak, giving rise to an increase of gallery distance by 0.2 nm from the gallery distance of 1.9 nm for Cloisite 30B and intercalation of Cloisite 30B aggregates as determined from TEM. The observed highly dispersed Cloisite 30B aggregates in PyHQ12/Cloisite 30B nanocomposite are attributed to the formation of hydrogen bonds, as determined by Fourier transform infrared spectroscopy, between the pendent pyridyl group in PyHQ12 and the hydroxyl groups in the surfactant MT2EtOH residing at the surface of Cloisite 30B. Oscillatory shear measurements of the three nanocomposites support the observations made from XRD and TEM.

1. Introduction

Since the publication of a series of papers in the early 1990s by the Toyota scientists[1] who prepared organoclay nanocomposites based on nylon-6, during the past decade well over several hundreds of papers[2] have been published in the literature dealing with the preparation of organoclay nanocomposites. Such efforts were based on the premise that a very high degree of dispersion of organoclay aggregates will generate very large surface areas, which then would significantly improve the mechanical properties of the nanocomposites. However, the expectation of achieving significantly improved mechanical properties in organoclay nanocomposites has not been realized to a large extent. Some of the improvement in mechanical properties, which was observed early on the organoclay nanocomposites based on nylon-6, is now understood as being not entirely due to the high degree of dispersion of organoclay aggregates, but due to the modification of the morphology of the nylon matrix in the presence of the organoclay.[3] On the other hand, highly dispersed organoclay nanocomposites have been found to increase heat distortion temperature[4] and the gas barrier properties (i.e., to decrease gas permeability).[5] Therefore, there still are sufficient incentives for preparing highly dispersed organoclay nanocomposites. For such purposes, two fundamental issues must be addressed.

The first issue to be addressed is to achieve compatibility between the thermoplastic polymer matrix and organoclay to obtain highly dispersed nanocomposites. It is well accepted that natural clay, perhaps with some exceptions, is not suitable for preparing highly dispersed nanocomposites. For this reason, during the past decade much effort has been spent on the development of surfactants that can modify the surface of natural clay. But, no general-purpose surfactant exists that can modify the surface of natural clay, which then enables one to prepare highly dispersed nanocomposites based on any thermoplastic polymer. Thus, more often than not, one must also modify the chemical structure of the thermoplastic polymer.

The second issue to be addressed is the preparation methods for nanocomposites. Two methods have widely been employed. One method is in-situ polymerization of monomer in the presence of an organoclay. While this method tends to produce highly dispersed nanocomposites, it is not always possible to adopt this method for the situations where polymers are already synthesized without an organoclay and when the presence of an organoclay interferes with the polymerization of monomer(s) (e.g., in anionic polymerization). In such situations, one has no choice but to prepare nanocomposites by mechanical mixing.

In the past, organoclay nanocomposites were prepared by either melt blending or solution blending using different thermoplastic polymers, namely, nylon-6,[6,7] polypropylene,[8−12] polystyrene,[13−15] poly(ethylene oxide),[16−21] poly(ϵ-caprolactone),[22−26] polycarbonate,[27,28] poly(ethylene-*ran*-vinyl acetate-*ran*-vinyl alcohol),[29] poly(vinylpyridine),[30,31] and elastomeric

---

* To whom correspondence should be addressed. E-mail: cdhan@uakron.edu.

10.1021/ma051470m CCC: $33.50 © 2006 American Chemical Society
Published on Web 11/24/2005

block copolymers.[32−35] The majority of the studies referred to above failed to obtain highly dispersed nanocomposites, primarily because there was a lack of sufficient compatibility between the polymer matrix and organoclay employed. Only a few research groups[36,37] reported on the preparation of organoclay nanocomposites based on thermotropic liquid-crystalline polymers (TLCP), but they observed intercalation of organoclay aggregates owing to the lack of sufficient compatibility between the TLCP and organoclay employed.

The objective of this study was to prepare and characterize highly dispersed organoclay nanocomposites based on a TLCP having a pendent functional group. For the study, we synthesized a TLCP having a pendent pyridyl group with the chemical structure (which hereafter will be referred to as PyHQ12)

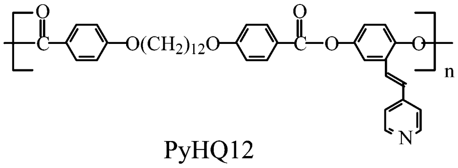

PyHQ12

The rationale behind the synthesis of PyHQ12 lies in the expectation that the pendent pyridyl group in PyHQ12 may form hydrogen bonds with the polar group in a surfactant residing at the surface of an organoclay, giving rise to highly dispersed nanocomposites. For comparison, we also synthesized a TLCP with the chemical structure (which hereafter will be referred to as PSHQ12)

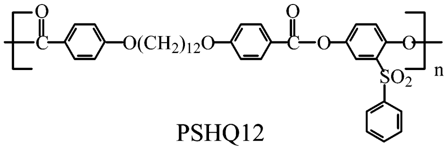

PSHQ12

Notice that the chemical structure of the backbone of PSHQ12 is exactly the same as that of PyHQ12. Using PyHQ12 and PSHQ12, we prepared nanocomposites with two different organoclays: one with hydroxyl groups and the other without polar groups. We have investigated (i) dispersion characteristics of the nanocomposites prepared using X-ray diffraction (XRD) and transmission electron microscopy (TEM), (ii) thermal transitions in the nanocomposites using differential scanning calorimetry (DSC), (iii) mesophase structure of the nanocomposites using polarized optical microscopy (POM), (iv) the presence of hydrogen bonds between the pendent pyridyl group in PyHQ12 and the hydroxyl groups in an organoclay using Fourier transform infrared (FTIR) spectroscopy, and (v) the dynamic linear viscoelasticity of the nanocomposites using oscillatory shear rheometry. In this paper we report the highlights of our findings.

2. Experimental Section

Synthesis of Liquid-Crystalline Polymers. In this study we synthesized two segmented main-chain TLCPs: one having pendent pyridyl groups (PyHQ12) and the other having a pendent phenylsulfonyl group (PSHQ12). The chemical structures of the two TLCPs are presented above. The synthesis procedures for PSHQ12 have been described in the literature,[38,39] and the synthesis procedures for PyHQ12 are described by Sato et al.[40] and summarized in the Supporting Information.

Preparation of Organoclay Nanocomposite Based on PyHQ12 or PSHQ12. To prepare nanocomposites based on PyHQ12 or PSHQ12, we employed natural clay, montmorillonite (MMT), and two commercial organoclays (Southern Clay Products): (i) Cloisite 30B treated with a surfactant (MT2EtOH) having the chemical structure methylbis-2-hydroxyethyltallow alkyl quaternary ammonium chloride and (ii) Cloisite 20A treated with a surfactant (2M2HT) having the chemical structure dimethyldihydrogenated tallow alkyl quaternary ammonium chloride. The chemical structures of the surfactants, MT2EtOH and 2M2HT, are[41]

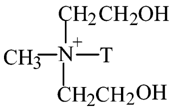

$$CH_3-\overset{\displaystyle CH_2CH_2OH}{\underset{\displaystyle CH_2CH_2OH}{\overset{+}{N}}}-T$$

MT2EtOH

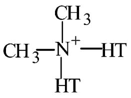

$$CH_3-\overset{\displaystyle CH_3}{\underset{\displaystyle HT}{N^+}}-HT$$

2M2HT

In the chemical structure of MT2EtOH, N^+ denotes a quaternary ammonium chloride and T denotes tallow consisting of ca. 65% C18, ca. 30% C16, and ca. 5% C14, and in the chemical structure of 2M2HT, N^+ denotes quaternary ammonium chloride and HT denotes hydrogenated tallow consisting of ca. 65% C18, ca. 30% C16, and ca. 5% C14. Note that 100% of Na^+ ions in natural clay (montmorillonite, MMT) have been exchanged.[41] Note that Cloisite 30B has hydroxyl groups while Cloisite 20A does not, as confirmed by FTIR spectroscopy.[29] The reason for having chosen these two organoclays lies in that we were interested in demonstrating that compatibility, via specific interactions, between a TLCP and an organoclay is necessary to achieve a very high degree of dispersion of organoclay aggregates. We prepared organoclay nanocomposites by solution blending; namely, a predetermined amount of PyHQ12 or PSHQ12 was dissolved in pyridine, and then an organoclay suspended in pyridine was added slowly, while vigorously stirring, into the polymer solution. The solvent in the mixture was evaporated slowly under constant stirring for 2 days. The mixture of PyHQ12 or PSHQ12 with an organoclay was dried completely in a vacuum oven at temperatures well above the boiling point of pyridine and also at ca. 20 °C above the glass transition temperature (T_g) of PyHQ12 or PSHQ12 until no weight changes were detected. The amount of organoclay used was 5 wt % in all nanocomposites. Since the amount of surfactant MT2EtOH (or 2M2HT) residing at the surface of Cloisite 30B (or Cloisite 20A) is 32 wt %, the net amount of clay was 3.4 wt % in each nanocomposite. For comparison, we also prepared PyHQ12/MMT nanocomposite, in which the amount of MMT used was 5 wt %.

According to the Technical Properties Bulletin[41] from Southern Clay Products, the amount of surfactant MT2EtOH residing at the surface of Cloisite 30B is 90 mequiv/100 g and the amount of surfactant 2M2HT residing at the surface of Cloisite 20A is 95 mequiv/100 g. Using methanol, we washed the organoclays, before use, to remove any excess surfactant.

X-ray Diffraction (XRD). Wide-angle X-ray scattering was conducted at ambient temperature on a Rigaku Rotaflex rotating anode diffractometer with slit collimation. The X-ray generator was operated at 40 kV and 150 mA, and the X-ray beam was monochromatized to Cu Kα with a graphite crystal. The range of 2θ scanning of X-ray intensity employed was 1.5°−10°. XRD patterns were obtained to determine the mean interlayer spacing of the (001) plane (d_{001}) for the organoclay (Cloisite 20A or Cloisite 30B) and its nanocomposites with PyHQ12 or PSHQ12.

Transmission Electron Microscopy (TEM). TEM images of specimens were taken at room temperature. The ultrathin sectioning (50−70 nm) of specimens was performed by ultramicrotomy at room temperature for the nanocomposites based on PyHQ12 or PSHQ12. A transmission electron microscope (JEM1200EX 11, JEOL) operated at 120 kV was used to obtain images of the nanocomposite specimens.

Oscillatory Shear Rheometry. An Advanced Rheometric Expansion System (ARES, TA Instruments) was used in the oscillatory mode with parallel plate fixtures (8 mm diameter). Dynamic temperature sweep experiments under isochronal conditions were conducted; i.e., the dynamic storage modulus (G') and dynamic loss modulus (G'') were measured at an angular frequency (ω) of 0.1 rad/s during heating, and the complex viscosity ($|\eta^*|$) was calculated using the expression $|\eta^*(\omega)| = \{[G'(\omega)/\omega]^2 +$

$[G''(\omega)/\omega]^2\}^{1/2}$. We also conducted dynamic frequency sweep experiments using a parallel plate fixture (8 mm diameter), measuring G' and G'' as functions of ω (ranging from 0.01 to 100 rad/s) at various temperatures between 130 and 190 °C, for which a fixed strain of 0.04 was used to ensure that measurements were taken well within the linear viscoelastic range of the materials investigated. Data acquisition was accomplished with the aid of a microcomputer interfaced with the rheometer. The temperature control was satisfactory to within ±1 °C. All experiments were conducted under a nitrogen atmosphere to preclude oxidative degradation of the samples.

Fourier Transform Infrared (FTIR) Spectroscopy. Using a Fourier transform infrared spectrometer (16 PC FTIR, Perkin-Elmer), in-situ FTIR spectra were obtained at temperatures ranging from 25 to 180 °C for PyHQ12 and PyHQ12/Cloisite 30B nanocomposites. The temperature was measured at the sample surface and controlled to within ±1.0 °C using a proportional-integral-derivative controller. Specimens were maintained at a preset temperature for 5 min prior to data acquisition. FTIR spectra for other specimens were obtained at room temperature. Spectral resolution was maintained at 4 cm^{-1}. Dry nitrogen gas was used to purge the sample compartment to reduce the interference of water and carbon dioxide in the spectrum. Thin films suitable for FTIR spectroscopy were prepared by casting 2% (w/v) solution in pyridine directly on the KBr salt plate. The film thickness was adjusted, such that the maximum absorbance of any band was less than 1.0, at which the Beer−Lambert law is valid. Film specimens were slowly dried for 24 h in a fume hood until most of the solvent evaporated and then dried at 80 °C for a few days in a vacuum oven, and they were then stored in a vacuum oven until use.

Differential Scanning Calorimetry (DSC). The phase transition temperatures of the nanocomposites based on PyHQ12 or PSHQ12 were determined, via differential scanning calorimetry (Perkin-Elmer DSC-7 series), using indium as the calibration standard, at heating or cooling rates of 20 °C/min under a nitrogen atmosphere.

Polarized Optical Microscopy (POM). The mesophase structures of the liquid-crystalline phase of PyHQ12 and PSHQ12 were investigated, via POM, using a Leitz Laborlux 12 Pol S polarized optical microscope equipped with a hot stage (Instec) and a digital camera (Spot insight 2, Diagnostic Instrument Inc.). Specimens were cast from 1 wt % solution of neat PyHQ12, neat PSHQ12 or their nanocomposites on a slide glass to obtain a film of about 2−3 μm in thickness, which was then first dried in a fume hood and then in a vacuum oven. The heating and cooling rates employed were 3 °C/min. Images of POM were obtained after keeping a specimen at a preset temperature for at least 10 min.

3. Results and Discussion

3.1. Characteristics of PyHQ12 and PSHQ12.

Let us compare the characteristics of PyHQ12 with that of PSHQ12. Such comparison will help us to later interpret the differences in the dispersion characteristics and also in the rheological behavior between the organoclay nanocomposite based on PyHQ12 and the organoclay nanocomposite based on PSHQ12.

(a) Thermal Transition and Mesophase Structure of PyHQ12 and PSHQ12. Figure 1 gives the DSC thermograms for (a) PyHQ12 and (b) PSHQ12 at a scanning rate of 20 °C/min during heating and cooling cycles. Keep in mind that PyHQ12 and PSHQ12 are different in the chemical structure of pendent groups. The following observations are worth noting in Figure 1. (i) PyHQ12 has a T_g of 96 °C and a clearing temperature (T_{cl}) of 162 °C during heating. The POM image given in the inset of Figure 1a indicates that PyHQ12 has Schlieren texture at temperatures between 96 and 162 °C, and thus 162 °C represents the nematic-to-isotropic (N−I) transition temperature (T_{NI}). (ii) PSHQ12 has a T_g of 80.7 °C and a T_{cl} of 167 °C during heating. However, PSHQ12 has an additional endothermic peak appearing at 118.1 °C, which represents the melting temperature of the crystalline phase of PSHQ12. The POM image given in the inset of Figure 1b indicates that PSHQ12 also has Schlieren texture at temperatures between 118.1 and 167 °C. Thus, we conclude that PyHQ12 is a glassy nematic-forming TLCP, while PSHQ12 is a semicrystalline nematic-forming TLCP. In the Supporting Information, we have shown that both the T_g and T_{NI} of PyHQ12 are little affected by annealing for 6−48 h, whereas an annealing of PSHQ12 for 12−72 h gave rise to a new endothermic peak at 163 °C, signifying the presence of high-temperature melting crystal.[42,43]

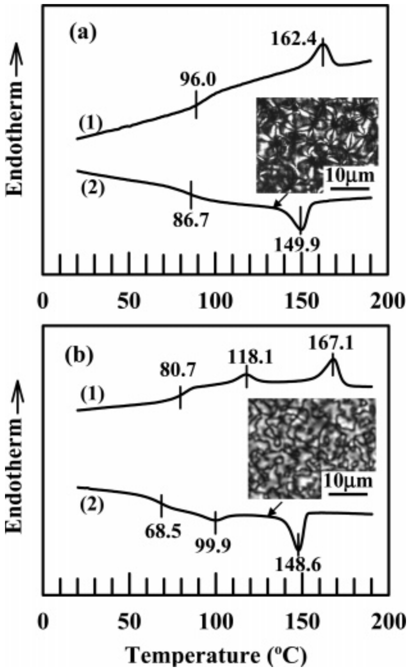

Figure 1. DSC thermograms for (a) PyHQ12 and (b) PSHQ12 at a scanning rate of 20 °C/min and their POM images at 130 °C.

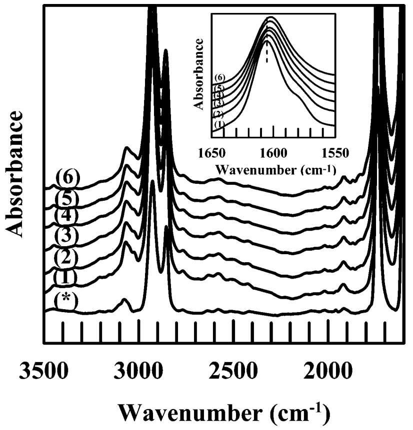

Figure 2. FTIR spectra for PSHQ12 denoted by (*) and in-situ FTIR spectra for PyHQ12 at various temperatures (°C): (1) 25, (2) 100, (3) 120, (4) 140, (5) 160, and (6) 180. The inset shows the absorption peaks at wavenumbers ranging from 1550 to 1650 cm^{-1}.

(b) FTIR Spectra of PyHQ12 and PSHQ12. Figure 2 gives in-situ FTIR spectra for PyHQ12 at various temperatures ranging from 25 to 180 °C and also, for comparison, the FTIR spectra for PSHQ12 (denoted by *) at room temperature. It can be seen in Figure 2 that PyHQ12 has two absorption peaks: a broad peak at a wavenumber of 2580 cm^{-1} and another at a wavenumber of 1920 cm^{-1}, both persisting over the entire range of temperatures tested. Let us review the polymerization mechanism (acidolysis) for PyHQ12 from *trans*-2′,5′-diacetoxy-4-stilbazole (monomer **1**) and 4,4′-dicarboxy-1,12-diphenoxy-

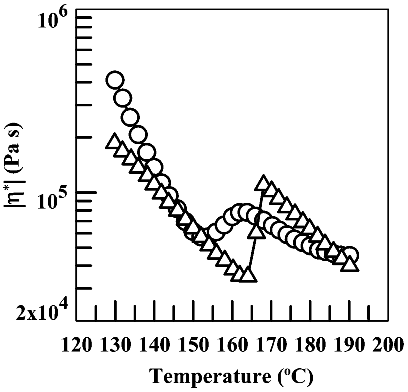

Figure 3. Variations of $|\eta^*|$ with temperature during isochronal dynamic temperature sweep experiments at ω = 0.1 rad/s for (○) PyHQ12 and (△) PSHQ12.

dodecane (monomer **2**) (see the Supporting Information for the chemical structures). It is well documented[44] that strong attractive interactions exist between pyridyl and carboxylic acid groups. After polymerization is completed, 50% of the terminal groups in PyHQ12 macromolecular chains could be carboxylic acid group. These terminal acid groups in PyHQ12 can form hydrogen bonds with the pendent pyridyl groups. The absorption peak at a wavenumber of 2580 cm^{-1} is believed to represent hydrogen bonds formed between the terminal carboxylic acid group in the main chain and pendent pyridyl group (i.e., self-association) in PyHQ12, while the absorption peak at a wavenumber of 1920 cm^{-1} represents the Fermi resonance. Also, in the inset of Figure 2 we observe that the absorption peak for pyridyl group at a wavenumber of 1606 cm^{-1} is shifted to a slightly lower wavenumber (1601 cm^{-1}) as the temperature is increased from 25 to 180 °C. This observation confirms that there actually exist hydrogen bonds between the terminal carboxylic acid group in the main chain and pendent pyridyl group of PyHQ12, the strength of which becomes weaker with increasing temperature. On the other hand, as expected, in Figure 2 there is no self-association in PSHQ12. The above observations are very important to interpret the differences in the dispersion characteristics of organoclay aggregates and also the differences in the rheological behavior between the nanocomposites based on PyHQ12 and the nanocomposites based on PSHQ12.

(c) Temperature Dependence of the Complex Viscosities of PyHQ12 and PSHQ12. Figure 3 describes the temperature dependence of complex viscosity ($|\eta^*|$) for PyHQ12 (○) and PSHQ12 (□), which were obtained from isochronal dynamic temperature sweep experiments at $\omega = 0.1$ rad/s. In Figure 3 we observe that values of $|\eta^*|$ for both PyHQ12 and PSHQ12 initially decrease with increasing temperature, going through a minimum, followed by an increase going through a maximum, and then decrease again with a further increase in temperature. Earlier, similar observations have been reported in the literature,[45] explaining that (i) the initial decrease of $|\eta^*|$ observed in Figure 3 is due to the orientation of the nematic mesophase during oscillatory shear, (ii) the increase of $|\eta^*|$ after passing through a minimum is due to the transition from the nematic to the isotropic phase, because the viscosity of the isotropic phase is higher than that of the nematic phase, and (iii) the decrease of $|\eta^*|$, after passing through a maximum, with a further increase of temperature is the characteristic of all homogeneous fluids following the Arrhenius relationship. Indeed, we observe in Figure 3 that the temperature at which values of $|\eta^*|$ go through a maximum is very close to the T_{NI} of the respective TLCPs, which were determined from the DSC thermograms given in Figure 1. However, referring to Figure 3, there is a significant difference between PyHQ12 and PSHQ12 in the ways how values of $|\eta^*|$ increase after passing through a minimum and decrease after passing through a maximum. Specifically, the values of $|\eta^*|$ for PyHQ12 increase rather slowly after passing through a minimum and decrease rather slowly after passing through a maximum, as compared to the values of $|\eta^*|$ for PSHQ12. We attribute this observation to a restricted mobility of PyHQ12 chains owing to self-association within the molecule, which arises from the hydrogen bonding between the terminal acid group in the main chain of PyHQ12 and the pendent pyridyl group (see the FTIR spectra given in Figure 2). This is in contrast to the situation for PSHQ12 that shows, referring to Figure 3, a very rapid increase in $|\eta^*|$ after passing a minimum and also a rapid decrease in $|\eta^*|$ after passing a maximum. After all, no self-association exists in PSHQ12 molecules.

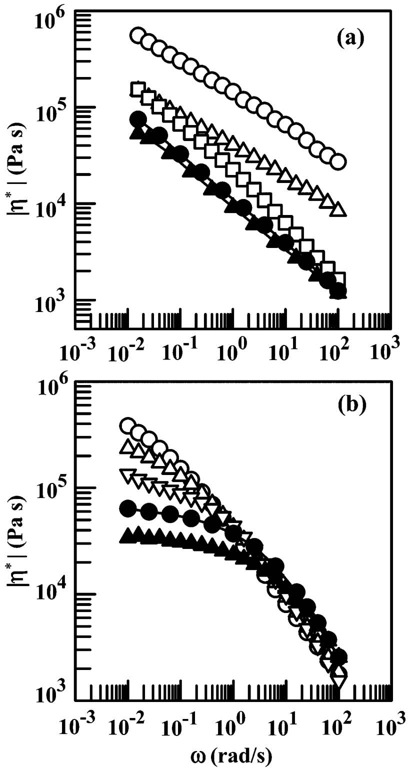

Figure 4. Plots of log $|\eta^*|$ vs log ω for (a) PyHQ12 and (b) PSHQ12 at various temperatures (°C): (○) 130, (△) 140, (□) 160, (▽) 165, (●) 180, and (▲) 190.

(d) Linear Dynamic Viscoelasticity of PyHQ12 and PSHQ12. Figure 4 gives log $|\eta^*|$ vs log ω plots for (a) PyHQ12 and (b) PSHQ12 at various temperatures ranging from 130 to 190 °C. The following observations are worth noting in Figure 4. (i) The $|\eta^*|$ of PyHQ12 exhibits shear-thinning behavior with almost the same slope at temperatures below T_{NI} (open symbols) and with a slightly steeper slope at temperatures above T_{NI} (filled symbols) over the entire range of ω applied from 10^{-2} to 10^2 rad/s. (ii) On the other hand, the $|\eta^*|$ of PSHQ12 exhibits shear-thinning behavior with varying slopes at temperatures below T_{NI} (open symbols) as ω increases from 10^{-2} to 10^2 rad/s and exhibits Newtonian behavior at low values of ω at temperatures above T_{NI} (filled symbols). Similar experimental observations, characteristics of all TLCPs without self-association, have also been reported previously.[39] What is significant in the frequency dependence of $|\eta^*|$ for PyHQ12 is that Newtonian behavior is not seen at temperatures above T_{NI}, which is attributable to the presence of self-association in PyHQ12.

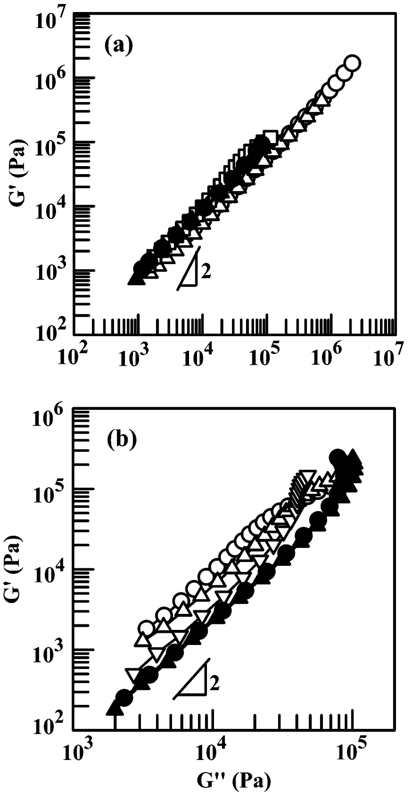

Figure 5. Plots of log G' vs log G'' for (a) PyHQ12 and (b) PSHQ12 at various temperatures (°C): (○) 130, (△) 140, (□) 160, (▽) 165, (●) 180, and (▲) 190.

Figure 5 gives log G' vs log G'' plots for (a) PyHQ12 and (b) PSHQ12 at various temperatures ranging from 130 to 190 °C. Figure 5 was prepared using the dynamic frequency sweep data obtained at various temperatures. For the sake of completeness, plots of log G' vs log ω and log G'' vs log ω at various temperatures are given in the Supporting Information for PyHQ12 and PSHQ12. The following observations are worth noting in Figure 5. (i) The log G' vs log G'' plots for PSHQ12 are shifted downward with increasing temperature in the nematic region (open symbols) and then become virtually independent of temperature in the isotropic region at 180 and 190 °C. Similar experimental observations, characteristics of all TLCPs without self-association, have also been reported previously.[46−48] (ii) However, the temperature dependence of log G' vs log G'' plots for PyHQ12 is quite different from that for PSHQ12; namely, the log G' vs log G'' plots in the nematic region (open symbols) for PyHQ12 show little temperature dependence, and the log G' vs log G'' plots in the isotropic region (filled symbols) lie above those in the nematic region (open symbols). In other words, the storage modulus G' in the isotropic state is greater than that in the nematic state. (iii) The slope of log G' vs log G'' plots in the terminal region is much less than 2 for PyHQ12, while it is close to 2 for PSHQ12. Note that the slope of log G' vs log G'' plots in the terminal region (at sufficiently low values of ω) is expected to be close to 2 for flexible homopolymers having no self-association.[49,50] Thus, we conclude that the very unusual temperature dependence of log G' vs log G'' plots observed for PyHQ12 in Figure 5a is attributable to the presence of self-association in PyHQ12.

3.2. Dispersion Characteristics and Rheology of Organoclay Nanocomposites Based on PyHQ12 or PSHQ12. **(a) XRD Patterns of Organoclay Nanocomposites Based on PyHQ12 or PSHQ12.** Figure 6 gives XRD patterns for Cloisite 20A, Cloisite 30B, and organoclay nanocomposites based on

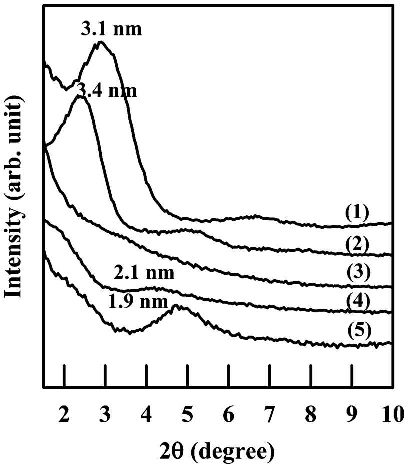

Figure 6. XRD patterns for (1) Cloisite 20A, (2) PyHQ12/Cloisite 20A nanocomposite, (3) PyHQ12/Cloisite 30B nanocomposite, (4) PSHQ12/Cloisite 30B nanocomposite, and (5) Cloisite 30B.

PyHQ12 or PSHQ12. Notice in Figure 6 that Cloisite 30B has a gallery distance (d_{001} spacing) of 1.9 nm, while Cloisite 20A has a d_{001} spacing of 3.1 nm. The following observations are worth noting in Figure 6. (i) PyHQ12/Cloisite 20A nanocomposite has a d_{001} spacing of 3.4 nm, an increase of 0.3 nm (9.7% increase) over the d_{001} spacing of Cloisite 20A, suggesting that the nanocomposite might have intercalated Cloisite 20A aggregates. (ii) PyHQ12/Cloisite 30B nanocomposite shows featureless XRD patterns. We hasten to point out that the disappearance of XRD peak does not necessarily signify that organoclay aggregates are highly dispersed. (iii) PSHQ12/Cloisite 30B nanocomposite has a d_{001} spacing of 2.1 nm, an increase of 0.2 nm (10.5% increase) over the d_{001} spacing of Cloisite 30B, suggesting that the nanocomposites might have intercalated Cloisite 30B aggregates. It is very clear from the above observations that PyHQ12/Cloisite 30B nanocomposite has XRD patterns, which are distinctly different from the XRD patterns of the two other organoclay nanocomposites, the origin of which will be elaborated on below. The XRD patterns for PyHQ12/MMT nanocomposite, showing little difference from the XRD patterns of MMT, are presented in the Supporting Information because they are not particularly interesting.

(b) TEM Images of Organoclay Nanocomposites Based on PyHQ12 or PSHQ12. Figure 7 gives TEM images of PyHQ12/Cloisite 30B, PyHQ12/Cloisite 20A, and PSHQ12/Cloisite 30B nanocomposites, in which the dark areas represent the organoclay and the gray/white areas represent the polymer matrix. It is clearly seen in Figure 7 that PyHQ12/Cloisite 30B nanocomposite has a very high degree of dispersion of Cloisite 30B aggregates in the matrix (PyHQ12), whereas PyHQ12/Cloisite 20A and PSHQ12/Cloisite 30B nanocomposites have large aggregates of organoclay, indicating poor dispersion of organoclay aggregates. We observe a correlation between the XRD patterns (see Figure 6) and the TEM images (see Figure 7). A TEM image of PyHQ12/MMT nanocomposite, showing very poor dispersion of MMT aggregates in the matrix PyHQ12, is presented in the Supporting Information because it is not particularly interesting. Such a poor dispersion of MMT aggregates in the matrix PyHQ12 can easily be understood from the point of view of the structure of MMT.[51,52]

(c) FTIR Spectra of Organoclay Nanocomposites Based on PyHQ12 or PSHQ12. Figure 8 gives FTIR spectra for (a) PyHQ12, (b) PyHQ12/Cloisite 20A nanocomposite, and (c) PSHQ12/Cloisite 30B nanocomposite at room temperature, showing slight evidence (spectrum b) of attractive interactions

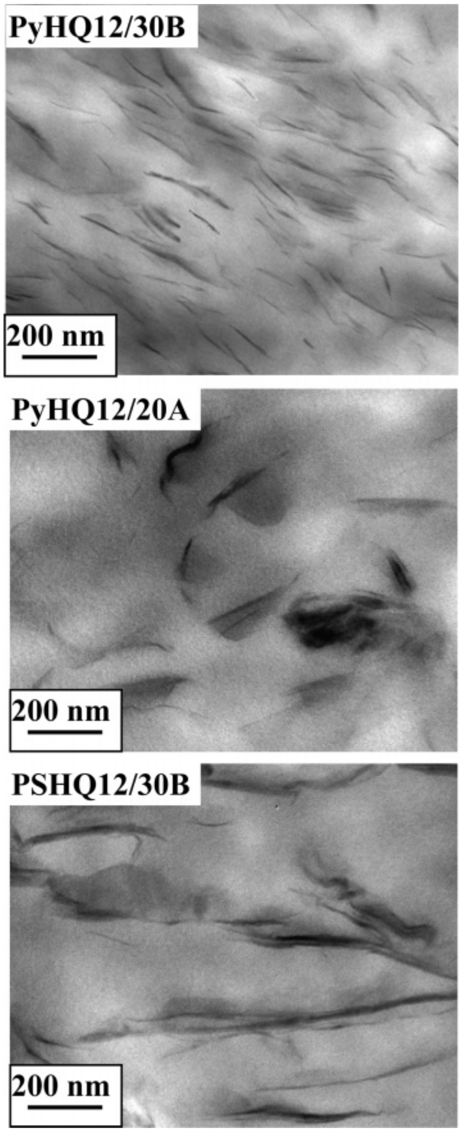

Figure 7. TEM images of PyHQ12/Cloisite 30B nanocomposite, PyHQ12/Cloisite 20A nanocomposite, and PSHQ12/Cloisite 30B nanocomposite, in which the dark areas represent the clay and the gray/white areas represent the polymer matrix.

between PyHQ12 and Cloisite 20A and no evidence (spectrum c) of attractive interactions between PSHQ12 and Cloisite 30B. This observation is not surprising, because organoclay Cloisite 20A does not have functional groups that can have attractive interactions with the pendent pyridyl group in PyHQ12, and PSHQ12 does not have functionality that can have attractive interactions with the hydroxyl group in the surfactant MT2EtOH residing at the surface of organoclay Cloisite 30B, although the hydroxyl group in MT2EtOH may have attractive interactions with the carbonyl group in PSHQ12,[53] which might have contributed to a slight increase in d_{001} spacing of Cloisite 30B in the PSHQ12/Cloisite 30B nanocomposite (Figure 6). Also given in Figure 8, for comparison, are in-situ FTIR spectra for PyHQ12/Cloisite 30B nanocomposite at various temperatures ranging from 25 to 180 °C. Notice in Figure 8 that the size of the absorption peak at a wavenumber of 2570 cm^{-1} for PyHQ12/Cloisite 30B nanocomposite is larger than that for PyHQ12 although it tends to decrease, while the size of the absorption peak at a wavenumber of 3460 cm^{-1} for the hydroxyl group tends to increase, as the temperature is increased to 180 °C. What is remarkable in the FTIR spectra for the PyHQ12/Cloisite 30B nanocomposite displayed in Figure 8 is that the rather strong absorption peak at a wavenumber of 2570 cm^{-1} persists even at a temperature as high as 180 °C. Thus, we can conclude that the attractive interactions exist (i.e., hydrogen bonds are formed) between the pendent pyridyl group in PyHQ12 and the hydroxyl group in the surfactant MT2EtOH residing at the surface of organoclay Cloisite 30B, which then helped achieve a very high degree of dispersion of Cloisite 30B aggregates in the matrix PyHQ12 (see the TEM image given in Figure 7). We hasten to point out that we cannot rule out the possibility of ionic interactions between the pendent pyridyl groups in PyHQ12 and N$^+$ ion in the surfactant 2M2HT residing at the surface of Cloisite 20A, contributing to a slight increase in d_{001} spacing of the PyHQ12/Cloisite 20A nanocomposite (see Figure 6).

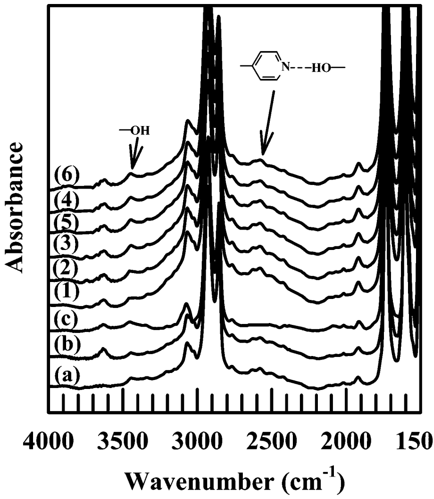

Figure 8. FTIR spectra for (a) PyHQ12, (b) PyHQ12/Cloisite 20A nanocomposite, (c) PSHQ12/ Cloisite 30B nanocomposite, and in-situ FTIR spectra for PyHQ12/Cloisite 30B nanocomposite at various temperatures (°C): (1) 25, (2) 100, (3) 120, (4) 140, (5) 160, and (6) 180.

FTIR spectra for PyHQ12/MMT nanocomposite were also obtained and they are presented in the Supporting Information because they are not particularly interesting. It can be seen that no evidence of attractive interactions exists between the pendent pyridyl group in PyHQ12 and MMT. This observation is not surprising because the terminal hydroxylated edge of the MMT apparently is not effective to form hydrogen bonds with the pendent pyridyl group in PyHQ12, as compared to the hydroxyl groups in the surfactant MT2EtOH residing at the surface of Cloisite 30B platelets. In other words, the hydroxyl groups in the surfactant MT2EtOH are distributed on the entire surface of the organoclay Cloisite 30B.

(d) Thermal Transition and Mesophase Structure of Organoclay Nanocomposites Based on PyHQ12 or PSHQ12. Figure 9 gives the DSC thermograms for PSHQ12/Cloisite 30B, PyHQ12/Cloisite 20A, and PyHQ12/Cloisite 30B nanocomposites at a heating rate of 20 °C/min. Comparison of Figure 9 with Figure 1 indicates that the T_{NI} of PyHQ12/Cloisite 30B nanocomposite is decreased by 8.7 °C, the T_{NI} of PyHQ12/Cloisite 20A nanocomposite is only slightly decreased (1.3 °C), and the T_{NI} of PSHQ12/Cloisite 30B nanocomposite is decreased by 3.7 °C. As shown in Table 1, the enthalpy of N−I transition, ΔH_{NI}, for the PyHQ12/Cloisite 30B nanocomposite is much smaller than that for neat PyHQ12, suggesting that the strength of liquid crystallinity of PyHQ12 in the PyHQ12/Cloisite 30B nanocomposite is decreased considerably in the presence of Cloisite 30B. On the other hand, the ΔH_{NI} for the PSHQ12/Cloisite 30B nanocomposite is only slightly smaller than that

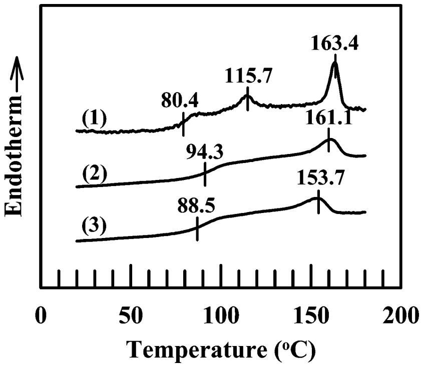

Figure 9. DSC thermograms for (1) PSHQ12/Cloisite 30B nanocomposite, (2) PyHQ12/Cloisite 20A nanocomposite, and (3) PyHQ12/Cloisite 30B nanocomposite at a heating rate of 20 °C/min.

Table 1. Enthalpy of N−I Transition, ΔH_{NI}, for PyHQ12, PSHQ12, and Their Organoclay Nanocomposites

sample code	ΔH_{NI} (J/g)
PyHQ12	3.80
PSHQ12	4.05
PyHQ12/Cloisite 30B	2.83
PyHQ12/Cloisite 20A	3.37
PSHQ12/Cloisite 30B	3.94

for neat PSHQ12, indicating that the strength of liquid crystallinity of PSHQ12 in the PSHQ12/Cloisite 30B nanocomposite is little affected by the presence of organoclay Cloisite 30B. Notice in Table 1 that the difference in ΔH_{NI} between the PyHQ12/Cloisite 30B and PSHQ12/Cloisite 30B nanocomposites is very large, while the difference in ΔH_{NI} between PyHQ12 and PSHQ12 is rather small. In Figure 8 we already have observed the presence of strong attractive interactions (i.e., the formation of hydrogen bonds) between the pendent pyridyl group in PyHQ12 and the hydroxyl groups in the surfactant MT2EtOH residing at the surface of Cloisite 30B, while little or no attractive interaction is present between the pendent phenylsulfonyl group in PSHQ12 and the surfactant MT2EtOH. Thus, we can conclude that the much smaller value of ΔH_{NI} for the PyHQ12/Cloisite 30B nanocomposite, as compared to the ΔH_{NI} for neat PyHQ12, is attributable to the presence of hydrogen bonds between the pendent pyridyl group in PyHQ12 and the hydroxyl groups in the surfactant MT2EtOH residing at the surface of Cloisite 30B. DSC thermograms and POM image of PyHQ12/MMT nanocomposite are presented in the Supporting Information, showing that the MMT in the nanocomposite has affected little the thermal transition temperatures and the mesophase structure of PyHQ12 (compare with Figure 1a). This observation confirms, once again, the results of XRD patterns, TEM image, and FTIR spectra presented in the Supporting Information.

Figure 10 gives POM images of PyHQ12/Cloisite 30B, PyHQ12/Cloisite 20A, and PSHQ12/Cloisite 30B nanocomposite. In Figure 10 we observe that a considerable degree of liquid crystallinity of PyHQ12 is lost in the PyHQ12/Closite 30B nanocomposite, which is attributable to the formation of hydrogen bonds between the pendent pyridyl group in PyHQ12 and the hydroxyl group in the surfactant MT2EtOH residing at the surface of Cloisite 30B.

Figure 11 gives a schematic describing the state of dispersion of Cloisite 30B aggregates in the PyHQ12/Cloisite 30B nanocomposite, where the dark sticks represent Cloisite 30B platelets, the thin cylinders (which denote mesogens) plus waved lines (which denote flexible spacers) represent the segmented PyHQ12 chains, and the short dashed lines represent hydrogen bonds between the pendent pyridyl group in PyHQ12 and the hydroxyl groups in the surfactant MT2EtOH residing at the surface of Cloisite 30B. Referring to Figure 11, the formation of hydrogen bonds between the pendent pyridyl group in PyHQ12 and the hydroxyl groups in the surfactant MT2EtOH might have restricted the mobility of PyHQ12 chains in the nanocomposite. As a result, the orientation of PyHQ12 chains in PyHQ12/Cloisite 30B nanocomposite is severely restricted, and thus the formation of nematic mesophase having long-range order of PyHQ12 would have become very difficult. Consequently, the domain size of PyHQ12 mesophase in PyHQ12/Cloisite 30B nanocomposite might have become very small, as shown in the POM image given in Figure 10.

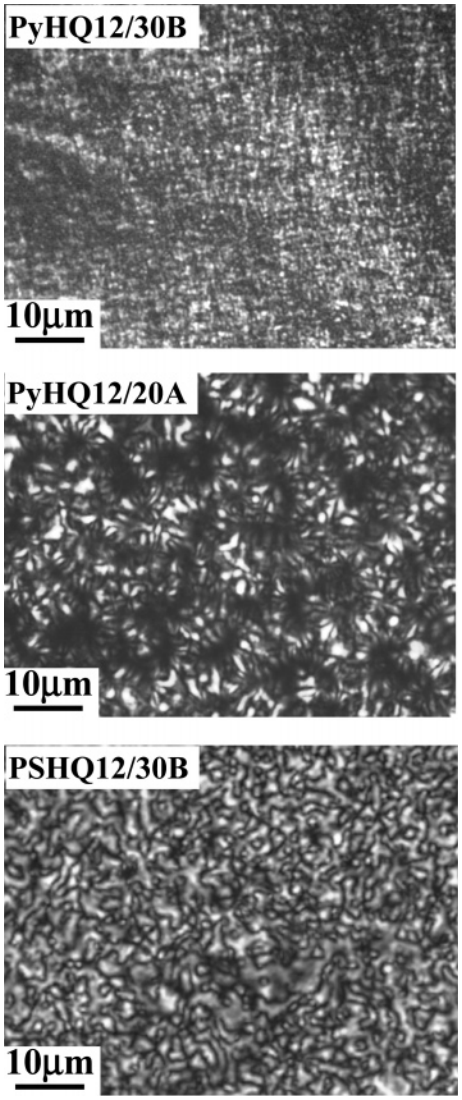

Figure 10. POM images of PyHQ12/Cloisite 30B nanocomposite, PyHQ12/Cloisite 20A nanocomposite, and PSHQ12/Cloisite 30B nanocomposite at 140 °C.

On the other hand, the nematic mesophase of PSHQ12 in the PSHQ12/Cloisite 30B nanocomposite (see Figure 10) is virtually identical to that of neat PSHQ12 (see Figure 1). This observation is not surprising because little or no attractive interactions exist between PSHQ12 and Cloisite 30B in the nanocomposite (see FTIR spectrum c in Figure 8). Notice in Figure 10 that in the presence of Cloisite 20A the nematic mesophase of PyHQ12 in the PyHQ12/Cloisite 20A nanocomposite has been modified only slightly when compared with the nematic mesophase of neat PyHQ12 given in Figure 1. This

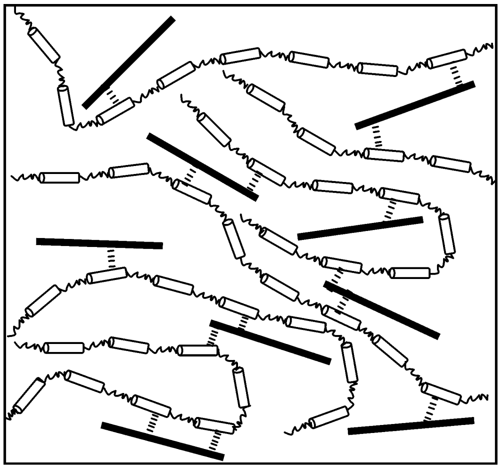

Figure 11. Schematic describing the distributions of PyHQ12 chains and organoclay Cloisite 30B in the highly dispersed PyHQ12/Cloisite 30B nanocomposite, where the dark sticks represent Cloisite 30B platelets, the thin cylinders (which denote mesogens) plus waved lines (which denote flexible spacers) represent PyHQ12 chains, and the short dashed lines represent hydrogen bonds between the pendent pyridyl group in PyHQ12 and the hydroxyl groups in the surfactant MT2EtOH residing at the surface of Cloisite 30B.

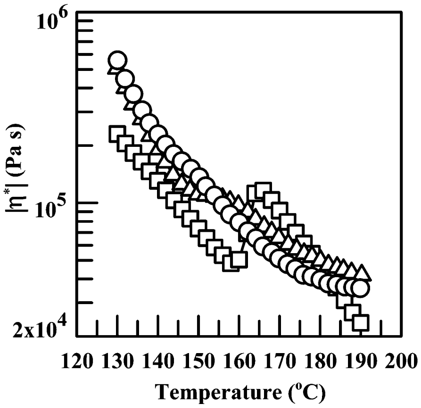

Figure 12. Variations of $|\eta^*|$ with temperature during isochronal dynamic temperature sweep experiments at $\omega = 0.1$ rad/s for (○) PyHQ12/Cloisite 30B nanocomposite, (△) PyHQ12/Cloisite 20A nanocomposite, and (□) PSHQ12/Cloisite 30B nanocomposite.

observation may be attributable to the possibility of having had very weak interactions between the pendent pyridyl group in PyHQ12 and the positively charged N^+ ion in the surfactant 2M2HT residing at the surface of organoclay Cloisite 20A.

(e) Temperature Dependence of the Complex Viscosity of Organoclay Nanocomposites Based on PyHQ12 and PSHQ12. Figure 12 describes the temperature dependence of $|\eta^*|$ for PyHQ12/Cloisite 30B, PyHQ12/Cloisite 20A, and PSHQ12/Cloisite 30B nanocomposites, which were obtained from isochronal dynamic temperature sweep experiments at $\omega = 0.1$ rad/s. It is instructive to compare Figure 12 with Figure 3. Namely, in Figure 12 we observe that values of $|\eta^*|$ for PyHQ12/Cloisite 30B nanocomposite decrease steadily with increasing temperature, and only a very narrow transition region can be discerned near its T_{NI} (ca. 154 °C as shown in Figure 9). On the other hand, in Figure 3 we observe that the $|\eta^*|$ for PyHQ12 first decreases, going through a minimum, followed by an increase going through a maximum at T_{NI}, and then decreases again with a further increase in temperature. In other words, the liquid crystallinity of PyHQ12 in the PyHQ12/Cloisite 30B nanocomposite is partially lost, which is consistent with the observation made from the POM image given in Figure 10. That is, the formation of hydrogen bonds in the PyHQ12/Cloisite 30B nanocomposite has disrupted the orientation characteristics of PyHQ12, while giving rise to a very high degree of dispersion of Cloisite 30B aggregates in the nanocomposite.

Comparison of Figure 12 with Figure 3 indicates that the temperature dependence of $|\eta^*|$ for PSHQ12/Cloisite 30B nanocomposite is virtually identical to that for neat PSHQ12. This makes sense because the mesophase structure of PSHQ12 in the PSHQ12/Cloisite 30B nanocomposite is little different from that of neat PSHQ12 (compare Figure 10 with Figure 1) and little attractive interactions exist between PSHQ12 and the surfactant MT2EtOH residing at the surface of Cloisite 30B (see Figure 8 for FTIR spectra). Notice in Figure 12 that the $|\eta^*|$ for PyHQ12/Cloisite 20A nanocomposite initially decreases rapidly with increasing temperature to ca. 145 °C, remains more or less constant as the temperature is increased to ca. 160 °C, and then decreases again with a further increase in temperature. The absence of an increasing trend of $|\eta^*|$ at temperatures between 145 and 165 °C in the PyHQ12/Cloisite 20A nanocomposite suggests that liquid crystallinity of PyHQ12 in PyHQ12/Cloisite 20A nanocomposite is disrupted somewhat, although not as much as that in PyHQ12/Cloisite 30B nanocomposite.

(f) Linear Dynamic Viscoelasticity of Organoclay Nanocomposites Based on PyHQ12 and PSHQ12. Figure 13 gives log $|\eta^*|$ vs log ω plots for PyHQ12/Cloisite 30B, PyHQ12/Cloisite 20A, and PSHQ12/Cloisite 30B nanocomposites at various temperatures ranging from 130 to 190 °C. PyHQ12/Cloisite 30B nanocomposite shows shear-thinning behavior over the entire range of ω ($10^{-2}-10^2$ rad/s) applied at all temperatures investigated. Comparison of Figure 13a with Figure 4a indicates that values of $|\eta^*|$ at low angular frequencies are much greater for PyHQ12/Cloisite 30B nanocomposite than for neat PyHQ12. The driving force giving rise to such strong shear-thinning behavior of PyHQ12/Cloisite 30B nanocomposite is the attractive interactions between PyHQ12 and organoclay Cloisite 30B, while the driving force giving rise to shear-thinning behavior of neat PyHQ12 is self-association within the molecules.

Comparison of Figure 13c with Figure 4b indicates that values of $|\eta^*|$ for PSHQ12/Cloisite 30B nanocomposite are virtually the same as those for neat PSHQ12. This observation is not surprising because little or no attractive interactions exist between PSHQ12 and Cloisite 30B in the nanocomposite (see FTIR spectrum c in Figure 8). The absence of attractive interactions in the PSHQ12/Cloisite 30B nanocomposite is further evidenced by the fact that at low values of ω Newtonian behavior is observed in Figure 13c.

In Figure 13b we observe that the temperature dependence of log $|\eta^*|$ vs log ω plots for PyHQ12/Cloisite 20A nanocomposite also show shear-thinning behavior over the entire range of ω applied, very similar to that for PyHQ12/Cloisite 30B nanocomposite, except for that values of $|\eta^*|$ for PyHQ12/Cloisite 20A nanocomposite are lower than those for PyHQ12/Cloisite 30B nanocomposite. However, the temperature dependence of log $|\eta^*|$ vs log ω plots for PyHQ12/Cloisite 20A nanocomposite appears to be similar to that for PSHQ12/Cloisite 30B nanocomposite, although little or no hydrogen bonds exist between PyHQ12 and organoclay Cloisite 20A, as evidenced from the FTIR spectra given in Figure 8. Since in the PyHQ12/Cloisite 20A nanocomposite little or very weak attractive interactions exist between PyHQ12 and the surfactant 2M2HT

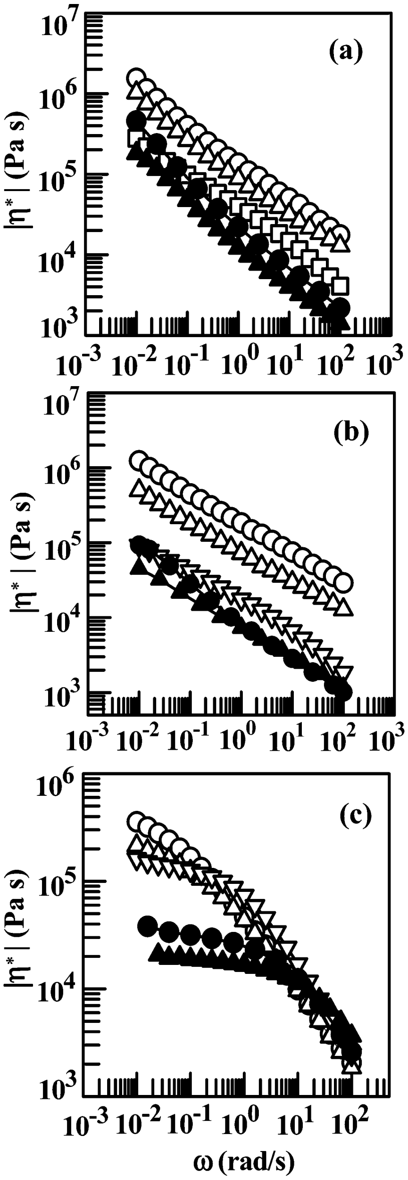

Figure 13. Plots of log $|\eta^*|$ vs log ω for (a) PyHQ12/Cloisite 30B nanocomposite, (b) PyHQ12/Cloisite 20A nanocomposite, and (c) PSHQ12/Cloisite 30B nanocomposite at various temperatures (°C): (○) 130, (△) 140, (□) 155, (▽) 160, (●) 180, and (▲) 190.

residing at the surface of Cloisite 20A (see the FTIR spectrum c in Figure 8), the frequency dependence of $|\eta^*|$ for the PyHQ12/Cloisite 20A nanocomposite, observed in Figure 13b, is primarily due to the frequency dependence of $|\eta^*|$ for neat PyHQ12 (see Figure 4a).

Figure 14 gives the log G' vs log G'' plots for PyHQ12/Cloisite 30B, PyHQ12/Cloisite 20A, and PSHQ12/Cloisite 30B nanocomposites at various temperatures ranging from 130 to 190 °C. Figure 14 was prepared from the results of dynamic frequency sweep experiments at various temperatures. Plots of G' vs log ω and G'' vs log ω are presented in the Supporting Information for PyHQ12/Cloisite 30B, PyHQ12/Cloisite 20A, and PSHQ12/Cloisite 30B nanocomposites. The following observations are worth noting in Figure 14. We observe a distinct difference in temperature dependence of log G' vs log G'' plots between PyHQ12/Cloisite 30B and PSHQ12/Cloisite 30B nanocomposites, while PyHQ12/Cloisite 30B and PyHQ12/Cloisite 20A nanocomposites have a similar temperature dependence of log G' vs log G'' plots. Specifically, the log G' vs log G'' plots for the PyHQ12/Cloisite 30B nanocomposite tend to move upward as the temperature is increased from 130 °C in the nematic region to 190 °C in the isotropic region (see Figure 9 for DSC thermograms), whereas the log G' vs log G'' plots for the PSHQ12/Cloisite 30B nanocomposite move downward as the temperature is increased from 130 °C in the nematic region to 190 °C in the isotropic region (see Figure 9 for DSC thermograms). In other words, for a fixed value of loss modulus G'', the storage modulus G' is higher in the isotropic region than in the nematic region for the PyHQ12/Cloisite 30B nanocomposite, which is quite opposite to the trend for the PSHQ12/Cloisite 30B nanocomposite. Earlier, similar observations were observed in organoclay nanocomposites based on a polystyrene-*block*-hydroxylated polyisoprene (SIOH diblock) copolymer,[34] in which the hydroxyl groups in the SIOH diblock copolymer underwent hydrogen bonding with the hydroxyl groups in the surfactant MT2EtOH residing at the surface of organoclay Cloisite 30B.

One may then ask why the PyHQ12/Cloisite 20A nanocomposite, which shows little or very weak interactions (see Figure 8), also shows the same trend of temperature dependence of log G' vs log G'' plots as the PyHQ12/Cloisite 30B nanocom-

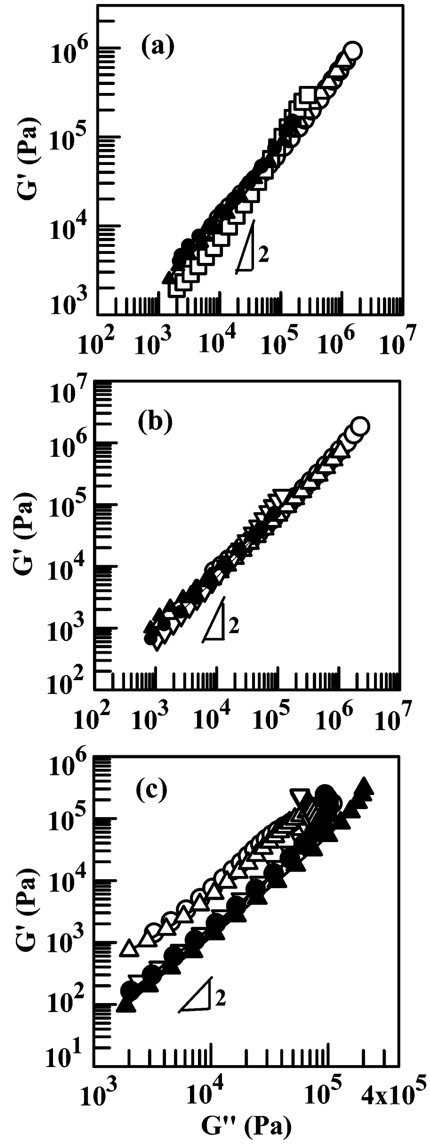

Figure 14. Plots of log G' vs log G'' for (a) PyHQ12/Cloisite 30B nanocomposite, (b) PyHQ12/Cloisite 20A nanocomposite, and (c) PSHQ12/Cloisite 30B nanocomposite at various temperatures (°C): (○) 130, (△) 140, (□) 155, (▽) 160, (●) 180, and (▲) 190.

posite does. As described above, it is quite possible to have very weak ionic interactions between the pendent pyridyl group in PyHQ12 and the positively charged N^+ ion in the surfactant 2M2HT residing at the surface of organoclay Cloisite 20A.

4. Concluding Remarks

Previously, two research groups[36,37] reported intercalation of organoclay aggregates in nanocomposites based on main-chain TLCPs. Such experimental observations are not surprising in that the TLCPs employed in both studies did *not* have any functionality. To demonstrate whether functionality is necessary to obtain highly dispersed nanocomposites based on TLCP, in this study we synthesized two main-chain TLCPs: one having pendent pyridyl group (PyHQ12) and the other having pendent phenylsulfonyl group (PSHQ12). Then, each TLCP was mixed with two different organoclays: one with hydroxyl groups (Cloisite 30B) and another without polar groups (Cloisite 20A). We have found that the PyHQ12/Cloisite 30B nanocomposite yielded a very high degree of dispersion of organoclay aggregates, while the PyHQ12/Cloisite 20A and PSHQ12/Cloisite 30B nanocomposites yielded a very low degree of dispersion of organoclay aggregates. The origin of the differences in the dispersion characteristics between PyHQ12/Cloisite 30B and PSHQ12/ Cloisite 30B nanocomposites and between PyHQ12/ Cloisite 30B and PyHQ12/Cloisite 20A nanocomposites is explained in terms of the attractive interactions, as determined by FTIR spectroscopy, between the pendent pyridyl group in PyHQ12 and the hydroxyl groups in the surfactant MT2EtOH residing at the surface of organoclay Cloisite 30B. We observed little or no attractive interactions between PSHQ12 and Cloisite 30B and between PyHQ12 and Cloisite 20A. These observations explain why the previous investigators[36,37] only observed intercalation of organoclay nanocomposites based on a TLCP without functionality.

We have observed a considerable loss in the degree of liquid crystallinity of PyHQ12 in the PyHQ12/Cloisite 30B nanocomposite, while the nanocomposite has a very high degree of dispersion of organoclay aggregates. We have explained this observation based on the argument that attractive interactions, via hydrogen bonding, between the pendent pyridyl group in PyHQ12 and the hydroxyl groups in the surfactant MT2EtOH residing at the surface of Cloisite 30B might have restricted the mobility of PyHQ12 chains in the nanocomposite, and consequently the orientation of the nematic mesophase might have been severely restricted. Note that the formation of hydrogen bonds between PyHQ12 and Cloisite 30B in the PyHQ12/Cloisite 30B nanocomposite is random in space (see Figure 11), making the orientation of PyHQ12 chains very difficult. Thus, we conclude that functionality in TLCP is necessary to obtain highly dispersed nanocomposites, but at the same time there is a possibility to lose some degree of liquid crystallinity in the TLCP. A challenge ahead us is to design and synthesize TLCP that would give rise to a very high degree of dispersion of organoclay aggregates without a loss in the degree of liquid crystallinity of the TLCP in organoclay nanocomposites prepared.

In this paper we have presented dramatic differences in linear dynamic viscoelasticity between PyHQ12/Cloisite 30B and PSHQ12/Cloisite 30B nanocomposites. The presence of hydrogen bonding in PyHQ12/Cloisite 30B nanocomposite is clearly demonstrated by the temperature dependence of complex viscosity (see Figure 12) and also by the temperature dependence of log G' vs log G'' plots (see Figure 14). We conclude that an investigation of linear dynamic viscoelasticity of organoclay nanocomposites based on TLCP is very useful to determine whether the TLCP employed is effective to achieve a high degree of dispersion of organoclay aggregates.

Acknowledgment. We acknowledge with gratitude that this study was supported in part by the National Science Foundation under Grant CST-04006752 and by LG Chemical Ltd. The organoclays employed were supplied by Southern Clay Products Inc., for which we are very grateful.

Note Added after ASAP Publication. The version of Supporting Information published ASAP November 24, 2005 was incorrect. The revised Supporting Information was published December 1, 2005.

Supporting Information Available: Synthesis procedures for PyHQ12, DSC thermograms for PyHQ12 and PSHQ12 specimens after extended annealing, the dispersion characteristics of PyHQ12/ MMT nanocomposite, the results of dynamic frequency sweep data (plots of log G' vs log ω and log G'' vs log ω) at various temperatures for PyHQ12, PSHQ12, and their nanocomposites, and TGA data for PyHQ12 and PSHQ12. This material is available free of charge via the Internet at http://pubs.acs.org.

References and Notes

(1) (a) Usuki, A.; Kawasumi, M.; Kojima, Y.; Okada, A.; Kurauchi, T.; Kamigaito, O. *J. Mater. Res.* **1993**, *8*, 1174. (b) Kojima, Y.; Usuki, A.; Kawasumi, M.; Okada, A.; Kurauchi, T.; Kamigaito, O. *J. Polym. Sci., Polym. Chem. Ed.* **1993**, *31*, 983. (c) Yano, K.; Usuki, A.; Okada, A.; Kurauchi, T.; Kurauchi, T.; Kamigaito, O. *J. Polym. Sci., Polym. Chem. Ed.* **1993**, *31*, 2493.

(2) Over several hundreds of references are listed under the title of “Clay Nanocomposites” in the Science Finder available on the Internet.

(3) Maiti, P.; Okamoto, M. *Macromol. Mater. Eng.* **2003**, *288*, 440.

(4) (a) Kojima, Y.; Usuki, A.; Kawasumi, M.; Okada, A.; Kurauchi, T.; Kamigaito, O. *J. Polym. Sci., Polym. Chem. Ed.* **1993**, *31*, 983. (b) Kojima, Y.; Usuki, A.; Kawasumi, M.; Okada, A.; Kurauchi, T.; Kamigaito, O. *J. Polym. Sci., Polym. Chem. Ed.* **1993**, *31*, 1775. (c) Kojima, Y.; Usuki, A.; Kawasumi, M.; Okada, A.; Furushima, Y.; Kurauchi, T.; Kamigaito, O. *J. Mater. Res.* **1993**, *8*, 1185.

(5) (a) Xu, R.; Mania, E.; Snyder, A. J.; Runt, J. *Macromolecules* **2001**, *34*, 337. (b) Hasegawa, N.; Okamoto, H.; Kato, M.; Usuki, A.; Sato, N. *Polymer* **2003**, *44*, 2933. (c) Raym, S.; Yamada, K.; Okamoto, N.; Ogami, A.; Ueda, K. *Chem. Mater.* **2003**, *15*, 1456.

(6) Hoffmann, B.; Kressler, J.; Stöppelmann, G.; Friedrich, C.; Kim, G.-M. *Colloid Polym. Sci.* **2000**, *278*, 629.

(7) Reynaud, E.; Jouen, T.; Gauthier, C.; Vigier, G.; Varlet, J. *Polymer* **2001**, *42*, 8759.

(8) Kato, M.; Usuki, A.; Okada, A. *J. Appl. Polym. Sci.* **1997**, *66*, 1781.

(9) Kawasumi, M.; Hasegawa, N.; Kato, M.; Usuki, A.; Okada, A. *Macromolecules* **1997**, *30*, 6333.

(10) Hasegawa, N.; Kawasumi, M.; Kato, M.; Usuki, A.; Okada, A. *J. Appl. Polym. Sci.* **1998**, *67*, 87.

(11) Liu, X.; Wu, Q. *Polymer* **2001**, *42*, 10013.

(12) Nam, P. H.; Maiti, P.; Okamoto, M.; Kotaka, T.; Hasegawa, N.; Usuki, A. *Polymer* **2001**, *42*, 9633.

(13) Sikka, M.; Cerini, L. N.; Ghosh, S. S.; Winey, K. I. *J. Polym. Sci., Polym. Phys. Ed.* **1996**, *34*, 1443.

(14) Hasegawa, N.; Okamoto, H.; Kawasumi, M.; Usuki, A. *J. Appl. Polym. Sci.* **1999**, *74*, 3359.

(15) Hoffmann, B.; Dietrich, C.; Thomann, R.; Friedrich, C.; Mülhaupt, R. *Macromol. Rapid Commun.* **2000**, *21*, 57.

(16) Ogata, N.; Kawakage, S.; Ogihara, T. *Polymer* **1997**, *38*, 5115.

(17) Liu, Y.-J.; Schindler, J. L.; DeGroot, D. C.; Kannewurf, C. R.; Hirpo, W.; Kanatzidis, M. G. *Chem. Mater.* **1996**, *8*, 525.

(18) Hou, S.-S.; Bonagamba, T. J. Beyer, F. L.; Madison, P. H.; Schmitdt-Rohr, K. *Macromolecules* **2003**, *36*, 2769.

(19) Zhang, Q.; Archer, L. A. *Langmuir* **2002**, *18*, 10435.

(20) Wu, J.; Lerner, M. M. *Chem. Mater.* **1993**, *5*, 835.

(21) Aranda, P.; Ruiz-Hitzky, E. *Chem. Mater.* **1992**, *4*, 1396.

(22) Messersmith, P. B.; Giannelis, E. P. *J. Polym. Sci., Polym. Chem. Ed.* **1995**, *33*, 1047.

(23) Jimenez, G.; Okata, N.; Kawai, H.; Ogihara, T. *J. Appl. Polym. Sci.* **1997**, *64*, 2211.

CDV

(24) Lepoittevin, B.; Pantoustier, N.; Devalckenaere, M.; Alexandre, M.; Kubies, D.; Calberg, E.; Jérôme, R.; Dubois, P. *Macromolecules* **2002**, *35*, 8385.
(25) Di, Y.; Iannace, S.; Di Maio, E.; Nicolais, L. *J. Polym. Sci., Polym. Phys. Ed.* **2003**, *41*, 670.
(26) Matti, P. *Langmuir* **2003**, *19*, 5502.
(27) Lee, K. M.; Han, C. D. *Polymer* **2003**, *44*, 4573.
(28) Yoon, P. J.; Hunter, D. L.; Paul, D. R. *Polymer* **2003**, *44*, 5323.
(29) Lee, K. M.; Han, C. D. *Macromolecules* **2003**, *36*, 7165.
(30) Fournaris, K. G.; Karakassides, M. A.; Petridis, D.; Yiannakopoulou, K. *Chem. Mater.* **1999**, *11*, 2372.
(31) Percy, M. J.; Barthet, C.; Lobb, J. C.; Khan, M. A.; Lascelles, S. F.; Vamvakaki, M.; Armes, S. P. *Langmuir* **2000**, *16*, 6913.
(32) Silva, A. S.; Mitchell, C. A.; Tse, M. F.; Wang, H.-C.; Krishnamoorti, R. *J. Chem. Phys.* **2001**, *115*, 7166.
(33) Krishnamoorti, R.; Silva, A. S.; Mitchell, C. A. *J. Chem. Phys.* **2001**, *115*, 7175.
(34) Lee, K. M.; Han, C. D. *Macromolecules* **2003**, *36*, 804.
(35) Choi, S.; Lee, K. M.; Han, C. D. *Macromolecules* **2004**, *37*, 7649.
(36) Vaia, R. A.; Giannelis, E. P. *Polymer* **2001**, *42*, 1281.
(37) Chang, J.-H.; Seo, B.-S.; Hwang, D.-H. *Polymer* **2002**, *43*, 2969.
(38) Furukawa, A.; Lenz, R. W. *Macromol. Chem., Macromol. Symp.* **1986**, *2*, 3.
(39) Kim, S. S.; Han, C. D. *Polymer* **1994**, *35*, 93.
(40) Sato, A.; Kato, T.; Uryu, T. *J. Polym. Sci., Polym. Chem. Ed.* **1996**, *34*, 503.
(41) Physical Properties Bulletin from Southern Clay Products, Inc.
(42) Kim, S. S.; Han, C. D. *Macromolecules* **1993**, *26*, 3176.
(43) Han, C. D.; Chang, S.; Kim, S. S. *Macromolecules* **1994**, *27*, 7699.
(44) (a) Kato, T.; Fréchet, J. M. J. *J. Am. Chem. Soc.* **1989**, *111*, 8533. (b) Pourcain, C. B. S.; Griffin, A. C. *Macromolecules* **1995**, *28*, 4116. (c) Cui, L.; Zhao, Y. *Chem. Mater.* **2004**, *16*, 2076. (d) Xu, J.; Toh, C. L.; Liu, X.; Wang, S.; He, C.; Lu, X. *Macromolecules* **2005**, *38*, 1684.
(45) Kim, S. S.; Han, C. D. *J. Polym. Sci., Polym. Phys. Ed.* **1994**, *32*, 371.
(46) Kim, C. D.; Han, C. D. *Macromolecules* **1993**, *26*, 6633.
(47) Kim, S. S.; Han, C. D. *J. Rheol.* **1993**, *37*, 847.
(48) Kim, D.-O.; Han, C. D. *Macromolecules* **2002**, *33*, 3349.
(49) Han, C. D.; Jhon, M. S. *J. Appl. Polym. Sci.* **1986**, *32*, 3809.
(50) Han, C. D. *J. Appl. Polym. Sci.* **1988**, *35*, 167.
(51) Grimm, R. E. *Clay Mineralogy*, 2nd ed.; McGraw-Hill: New York, 1968; Chapter 4.
(52) van Olphen, H. *Clay Colloid Chemistry*, 2nd ed.; John Wiley & Sons: New York, 1977; Chapter 5.
(53) During polymerization to obtain PSHQ12,[39] the diacid of monomer II was chlorinated, which then reacted with biphenol of monomer I. After the completion of polymerization, the polymer was precipitated in methanol. As a result, the acid chloride was terminated by methanol, and 50% of the terminal group should be the hydroxyl group of phenol. Therefore, there is no terminal acid group in PSHQ12. The attractive interactions, via hydrogen bonding, between the carbonyl groups in polycarbonate and the hydroxyl groups in MT2EtOH have been reported by Lee and Han.[27]

MA051470M